









High critical current density and high-tolerance superconductivity in high-entropy alloy thin films

Soon-Gil Jung ^{1,2,6}✉, Yoonseok Han ^{1,2,6}, Jin Hee Kim ^{3,4,6}, Rahmatul Hidayati ^{3,4}, Jong-Soo Rhyee ^{3,4}, Jung Min Lee ², Won Nam Kang², Woo Seok Choi ², Hye-Ran Jeon⁵, Jaekwon Suk⁵ & Tuson Park ^{1,2}✉

High-entropy alloy (HEA) superconductors—a new class of functional materials—can be utilized stably under extreme conditions, such as in space environments, owing to their high mechanical hardness and excellent irradiation tolerance. However, the feasibility of practical applications of HEA superconductors has not yet been demonstrated because the critical current density (J_c) for HEA superconductors has not yet been adequately characterized. Here, we report the fabrication of high-quality superconducting (SC) thin films of Ta-Nb-Hf-Zr-Ti HEAs via a pulsed laser deposition. The thin films exhibit a large J_c of >1 MA cm^{-2} at 4.2 K and are therefore favorable for SC devices as well as large-scale applications. In addition, they show extremely robust superconductivity to irradiation-induced disorder controlled by the dose of Kr-ion irradiation. The superconductivity of the HEA films is more than 1000 times more resistant to displacement damage than that of other promising superconductors with technological applications, such as MgB_2 , Nb_3Sn , Fe-based superconductors, and high- T_c cuprate superconductors. These results demonstrate that HEA superconductors have considerable potential for use under extreme conditions, such as in aerospace applications, nuclear fusion reactors, and high-field SC magnets.

¹Center for Quantum Materials and Superconductivity (CQMS), Sungkyunkwan University, Suwon 16419, Republic of Korea. ²Department of Physics, Sungkyunkwan University, Suwon 16419, Republic of Korea. ³Department of Applied Physics, Integrated Education Institute for Frontier Science and Technology (BK 21 Four), Kyung Hee University, Yongin 17104, Republic of Korea. ⁴Institute of Natural Science, Kyung Hee University, Yongin 17104, Republic of Korea. ⁵Korea Multi-purpose Accelerator Complex, Korea Atomic Energy Research Institute, Gyeongju, Gyeongbuk 38180, Republic of Korea. ⁶These authors contributed equally: Soon-Gil Jung, Yoonseok Han, Jin Hee Kim. ✉email: prosgjung@gmail.com; tp8701@skku.edu

High-entropy alloys (HEAs), which are typically composed of multiple metallic elements, open new avenues for the design of novel functional materials because they have superior physical and mechanical properties to conventional alloys^{1–8}. In general, HEAs have simple body-centered cubic (bcc), face-centered cubic (fcc), and hexagonal close-packed (hcp) structures^{3,4}, although five or more elements randomly occupy one available crystallographic position, with each element having an atomic fraction between 5 and 35%^{1,3}. Thermodynamically, a single phase solid solution in HEAs is considered due to a dominance of the entropy of mixing (ΔS_{mix}) in the Gibbs free energy difference, $\Delta G_{\text{mix}} = \Delta H_{\text{mix}} - T\Delta S_{\text{mix}}$, where T is the temperature and ΔH_{mix} is the enthalpy of mixing that contributes to phase separation or the formation of multi-component alloys^{3,4}. Because the elements have slightly different atomic sizes, the novel physical properties and high mechanical hardness of HEAs are believed to result from their large atomic disorder^{3,4,8}.

The superconductivity of HEAs was discovered in 2014 in Ta–Nb–Hf–Zr–Ti multi-principal element alloy, attracting considerable interest in their pairing mechanism; generally, a high level of disorder in crystalline superconductors limits the formation of Cooper pairs partially owing to the decrease in the density of states or the increase in effective Coulomb repulsion between paired electrons^{9,10}. In addition, the unique properties of HEAs, such as their high hardness, high strength, and excellent irradiation tolerance, are advantageous for use under extreme conditions such as those in aerospace applications, irradiation environments, and superconducting (SC) rotating machines^{2–4,6,11}. Recently, the robust superconductivity of Ta–Nb–Hf–Zr–Ti HEAs under extremely high pressures of approximately 190 GPa has been reported⁵, where the unit cell volume of Ta–Nb–Hf–Zr–Ti HEAs was expected to be considerably compressed by ~53%. Since the lattice constant of a crystal is closely related to its electronic structure, we believe that HEA superconductors are not only interesting for fundamental studies of pairing mechanism, but also promising for applications under extreme conditions¹². However, the critical current density (J_c), i.e., the maximum current density that can conduct electric current without any power dissipation, was reported to be 0.01–10 kA cm⁻² for Co–Ni–Cu–Rh–Ir–Zr and Ta–Nb–Hf–Zr–Ti HEA superconductors. This value is extremely low for practical applications^{13,14}.

Here, we report high- J_c Ta–Nb–Hf–Zr–Ti HEA SC thin films fabricated by pulsed laser deposition (PLD) and the extraordinarily robust superconductivity against irradiation-induced disorder verified using 200 keV Kr-ion irradiation. The HEA SC thin films were deposited on *c*-cut Al₂O₃ substrates over a wide range of substrate temperatures (T_s) from 270 to 620 °C. A film deposited at $T_s = 520$ °C showed the highest SC transition temperature ($T_c = 7.28$ K) and the largest J_c (>1 MA cm⁻²) at 4.2 K, which is promising for SC devices as well as large-scale applications. Moreover, the superconductivity of Ta–Nb–Hf–Zr–Ti HEA SC thin films was found to be approximately 1000 times more resistant to irradiation damage than that of other promising SC materials, including high- T_c cuprate superconductors. Taken together, these discoveries suggest that the HEA SC thin films possess considerable potential for technological applications under extreme conditions.

Results and discussion

Crystal structure and SC transition in HEA thin films. Figure 1a shows a schematic of the bcc crystal structure of Ta–Nb–Hf–Zr–Ti superconductors with a compositional ratio of Ta:Nb:Hf:Zr:Ti = 1:2:1:1:1, where each color represents the expected atomic fraction of each element occupying one crystallographic site. For instance, the Nb atom, which is indicated

by the green color, accounts for a fraction of 1/3, whereas Ta, Hf, Zr, and Ti each account for 1/6. The X-ray diffraction (XRD) patterns of θ – 2θ scans of the Ta–Nb–Hf–Zr–Ti HEA SC thin films fabricated on *c*-cut Al₂O₃ substrates indicated that all the films with the bcc crystal structure had a preferred orientation of (110), regardless of the substrate temperature (T_s), as shown in Fig. 1b. The inset of Fig. 1b shows a cross-sectional scanning electron microscopy (SEM) image of the film fabricated at $T_s = 520$ °C with a thickness of approximately 700 nm. The lattice parameter a_0 with respect to T_s for the HEA SC thin films are summarized in Fig. 1c, and the film deposited at $T_s = 520$ °C, which exhibits the highest XRD peak intensity, has $a_0 = 3.358$ Å, which is similar to that of bulk Ta_{1/6}Nb_{2/6}Hf_{1/6}Zr_{1/6}Ti_{1/6} HEA superconductors¹³. The slight peak shift and low intensity for the thin films fabricated at T_s values other than 520 °C are more closely related to the substrate temperature than the compositional ratio of the films^{15,16} (see Supplementary Table 1 and Supplementary Figs. 1–3).

Figure 1d presents the temperature dependence of the electrical resistivity (ρ) of the Ta–Nb–Hf–Zr–Ti HEA SC thin films grown at $T_s = 270, 370, 470, 520, 570,$ and 620 °C, where $\rho(T)$ is normalized to the ρ value at the T_c onset (ρ_n) for comparison. All the films exhibited a sharp SC transition, and the film fabricated at 520 °C showed the highest SC transition temperature ($T_c = 7.28$ K). Here, the T_c from the $\rho(T)$ curves (T_{cR}) was determined by the 50% transition of ρ_n , as indicated by the solid line and arrow in Fig. 1d. The bulk SC transition for the HEA SC thin films, which was investigated using zero-field-cooled (ZFC) and field-cooled (FC) dc magnetization (M), also showed similar trends to the $\rho(T)$ curves, as shown in Fig. 1e. All the films exhibited clear Meissner signals and sharp SC transitions in the ZFC $M(T)$ curves, reflecting their high quality. Here, $M(T)$ was normalized to the absolute ZFC M value at 1.8 K for comparison, and the T_c from the $M(T)$ curves (T_{cM}) was determined by the irreversible points of the ZFC and FC $M(T)$ curves, as indicated by the arrow representing the film deposited at the optimal $T_s = 520$ °C.

The dependence of the magnetic field of the SC phase transition is selectively displayed for the Ta–Nb–Hf–Zr–Ti HEA SC thin film deposited at the optimal $T_s = 520$ °C in Fig. 2a, where various magnetic fields from 0 to 9 T were applied perpendicularly to the film plane (see also Supplementary Fig. 4). Although the magnitude of the applied magnetic field increased, the SC transition of the HEA SC thin films did not broaden considerably, revealing that the HEA superconductor has a strong vortex pinning strength^{17,18}. In general, because the number of vortices is proportional to the magnetic field and the vortex motion generates an electric field, an increase in the magnetic field results in a broad SC transition in type-II superconductors with weak vortex pinning strengths^{19,20}.

Figure 2b shows the upper critical field ($\mu_0 H_{c2}$) as a function of the temperature for the HEA SC thin films, where $\mu_0 H_{c2}(T)$ was obtained from the $\rho(T, H)$ curves using the same criterion that was employed for T_{cR} (50% of ρ_n). The red dashed lines indicate the linear slope of H_{c2} near T_c for the films deposited at $T_s = 270$ and 520 °C, where $(dH_{c2}/dT)_{T=T_c} = -2.17, -2.44, -2.63, -2.41, -2.51,$ and -1.73 T K⁻¹ for the HEA SC thin films deposited at $T_s = 270, 370, 470, 520, 570,$ and 620 °C, respectively. The upper critical field at zero Kelvin, $\mu_0 H_{c2}(0)$, was evaluated using the Werthamer–Helfand–Hohenberg (WHH) formula in the dirty limit:²¹

$$\mu_0 H_{c2}^{\text{WHH}}(0) = -0.693 T_c (dH_{c2}/dT)_{T_c}. \quad (1)$$

The estimated $\mu_0 H_{c2}(0)$ values of the HEA SC thin films and the SC transition temperatures determined from the electrical resistivity (T_{cR}) and magnetization (T_{cM}) are displayed in Fig. 2c. It is observed that $\mu_0 H_{c2}(0)$ with respect to T_s exhibits a similar

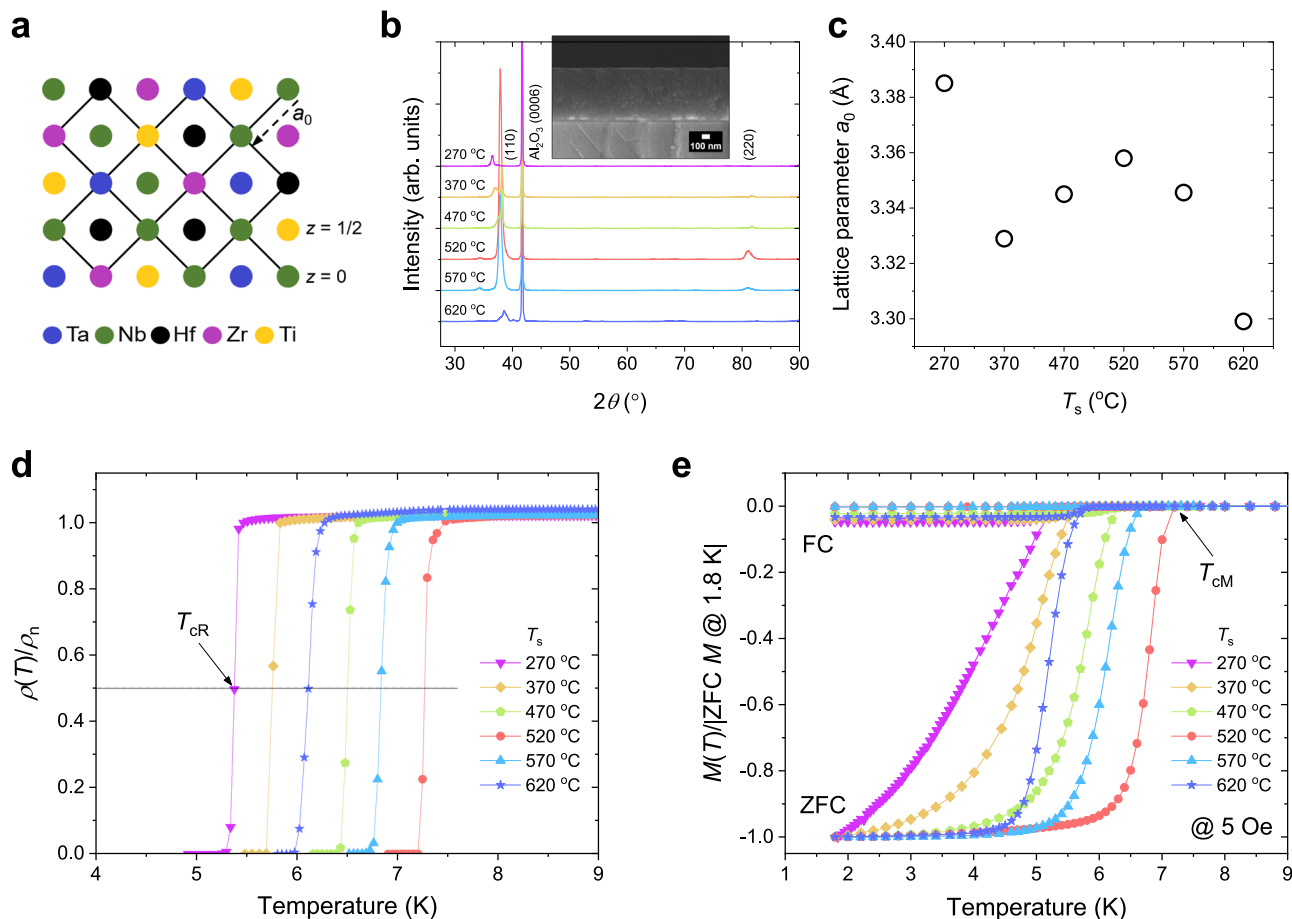


Fig. 1 Crystal structure and superconducting (SC) transition temperature of Ta-Nb-Hf-Zr-Ti HEA SC thin films. **a** Schematic of the bcc lattice with randomly distributed atoms of the $\text{Ta}_{1/6}\text{Nb}_{2/6}\text{Hf}_{1/6}\text{Zr}_{1/6}\text{Ti}_{1/6}$ HEA superconductor. **b** XRD results for Ta-Nb-Hf-Zr-Ti HEA SC thin films deposited on a c-cut Al_2O_3 substrate at $T_s = 270, 370, 470, 520, 570,$ and $620\text{ }^\circ\text{C}$, indicating a (110) preferred orientation. The inset shows a cross-sectional SEM image for the film fabricated at $T_s = 520\text{ }^\circ\text{C}$. **c** The lattice parameter (a_0) of HEA SC thin films with respect to substrate temperature T_s . **d, e** Temperature dependence of the electrical resistivity (ρ) and magnetization (M) for the Ta-Nb-Hf-Zr-Ti HEA SC thin films, respectively. Here, $\rho(T)$ and $M(T)$ were normalized to the ρ at the T_c onset (ρ_n) and the absolute zero-field-cooled (ZFC) M value at 1.8 K, respectively, for comparison. The field-cooled (FC) and ZFC $M(T)$ were measured at 5 Oe (applied perpendicularly to the film plane).

tendency to T_c , indicating that a higher T_c can induce a larger $\mu_0 H_{c2}(0)$ of the HEA SC thin films. However, the $\mu_0 H_{c2}(0)$ of the thin films fabricated at temperatures above the optimal $T_s = 520\text{ }^\circ\text{C}$ showed a more rapid reduction compared to the decrease in T_c . Despite the high T_c , small slope values of $(dH_{c2}/dT)_{T=T_c}$ have also been reported in $(\text{TaNb})_{1-x}(\text{HfZrTi})_x$ HEA superconductors by controlling the mixing entropy or application of pressure^{5,15,16}. Typically, because the SC coherence length (ξ) in dirty type-II superconductors is proportional to the mean free path (l) of the charge carriers, $H_{c2}(0)$ can be improved by adjusting the disorder level^{22,23}.

Critical current density of HEA SC thin films. Figure 3a and b show the magnetic field dependence of the critical current density (J_c) at 2.0 K and 4.2 K, respectively, for Ta-Nb-Hf-Zr-Ti HEA SC bulk and SC thin films deposited at different temperatures. The J_c data for the bulk sample are for the high-quality $\text{Ta}_{1/6}\text{Nb}_{2/6}\text{Hf}_{1/6}\text{Zr}_{1/6}\text{Ti}_{1/6}$ superconductor with $T_{cM} = 7.8\text{ K}$ used as the target for the deposition of HEA SC thin films in this study (see Supplementary Fig. 5a). All the films exhibited substantially larger J_c values than the bulk sample—particularly those grown at $T_s = 470, 520,$ and $570\text{ }^\circ\text{C}$ (see also Supplementary Fig. 5). For example, the magnitudes of J_c for a film deposited at the optimal $T_s = 520\text{ }^\circ\text{C}$, which had $J_c > 1\text{ MA cm}^{-2}$, were approximately 820 and 790% larger than those of

the bulk sample at 2.0 K (@ 3.4 T) and 4.2 K (@ 2 T), respectively. Here, the magnitude of $J_c(@ 0\text{ T})$ of the HEA SC thin films is comparable to that of the most widely used commercial superconductor NbTi alloy^{24–26}. A higher $J_c(@ 0\text{ T})$, i.e., self-field J_c , in SC thin films compared to bulk samples is commonly observed for most SC materials, including MgB_2 and high- T_c cuprates^{27,28}. This is thought to be because the self-field J_c is confined to the surface area associated with lower critical field (H_{c1}) and London penetration depth (λ) rather than distributed over the entire cross-sectional area^{28,29}. The strong field performance of J_c of the HEA SC thin films is considered to be closely associated with the intrinsic internal disorder caused by the slightly different atomic sizes of the constituent atoms (see Supplementary Fig. 6). The large reduction in the low-field J_c at 2.0 K resulted from the large flux jump due to thermal instability (see Supplementary Fig. 7)^{30,31}, indicating that the J_c of the HEA SC thin films can be further improved³². The red dashed lines indicate $J_c = 0.1\text{ MA cm}^{-2}$, which is a common benchmark for large-scale practical applications of superconductors such as high-field SC magnets³³. Relative magnitudes of J_c at 2.0 and 4.2 K at 1 T were described in Fig. 3c. The large J_c values over a wide range of film growth temperatures suggest that HEA superconducting thin films not only have considerable potential for SC devices, but also can replace conventional SC alloys in practical engineering applications.

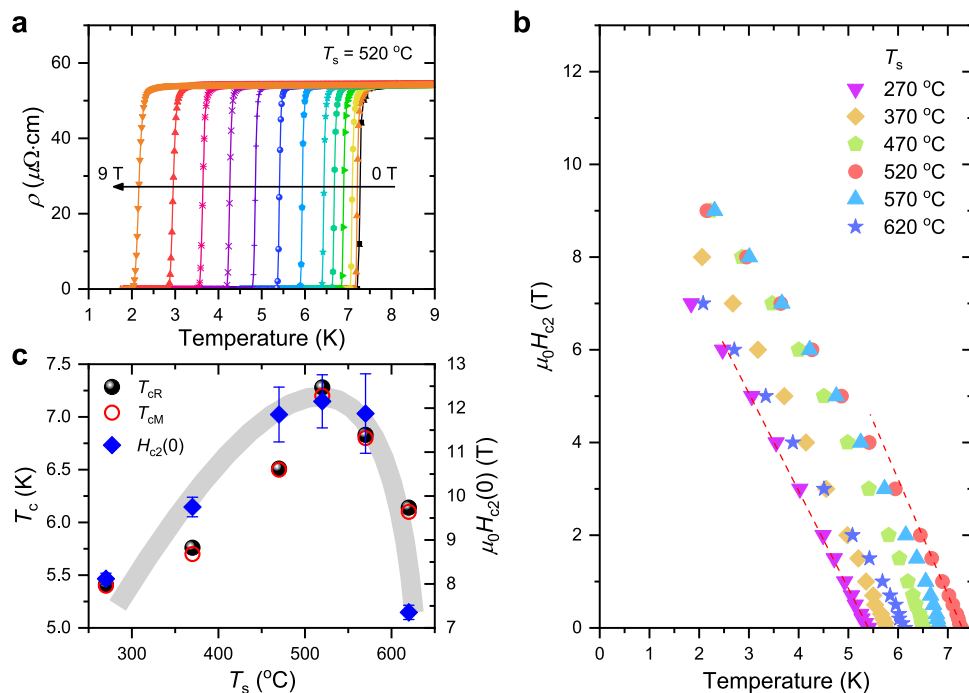


Fig. 2 Upper critical fields and SC transition temperatures of HEA SC thin films with respect to the growth temperature. **a** Representative $\rho(T)$ curves under various magnetic fields ranging from 0 to 9 T for the HEA SC thin film fabricated at the optimal $T_s = 520$ °C, where the direction of the applied magnetic field was perpendicular to the ab plane of the films. **b** Upper critical field ($\mu_0 H_{c2}$) as a function of the temperature for the HEA SC thin films, determined by 50% of the SC transition from the ρ_n at each magnetic field. Red dashed lines for $T_s = 270$ and 520 °C indicate representative linear fits for the estimation of dH_{c2}/dT near T_c . **c** T_c and $\mu_0 H_{c2}$ at zero Kelvin, $\mu_0 H_{c2}(0)$, with respect to the substrate temperature T_s . Here, T_{cR} and T_{cM} were determined by the 50% transition of ρ_n and the irreversible points of the ZFC and FC $M(T)$ curves, respectively, and the $\mu_0 H_{c2}(0)$ was estimated using the Werthamer-Helfand-Hohenberg model. T_c and $\mu_0 H_{c2}(0)$ exhibit a similar behavior with respect to T_s , implying that the high T_c of HEA SC thin films leads to a large $\mu_0 H_{c2}(0)$. The error bars on the $\mu_0 H_{c2}(0)$ reflect the uncertainties in the linear fitting of dH_{c2}/dT around T_c . Half-transparent shades are guides to the eyes.

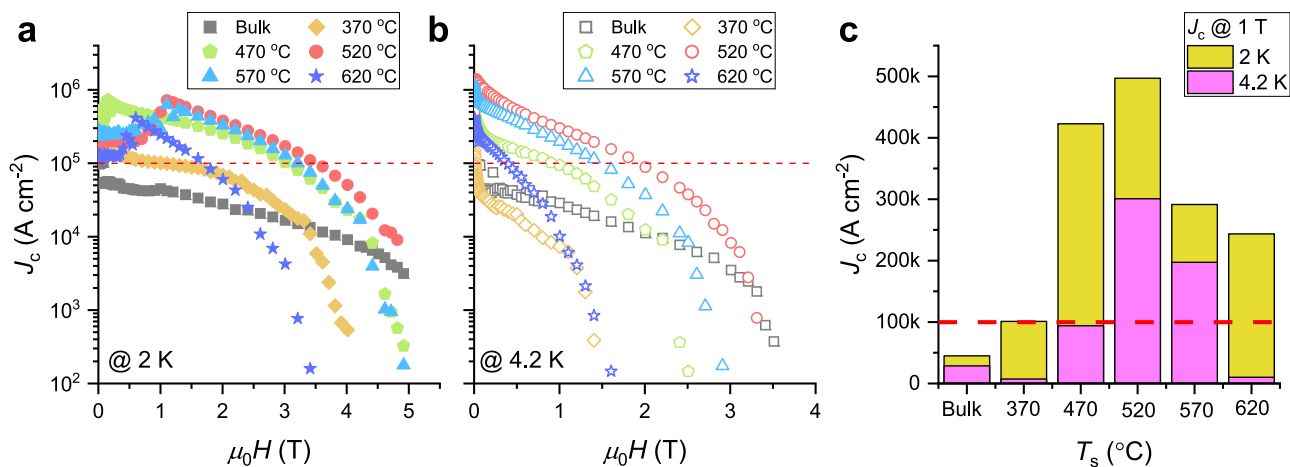


Fig. 3 Magnetic field dependence of the critical current density for Ta-Nb-Hf-Zr-Ti HEA SC thin films. **a, b** Magnetic field dependence of the critical current density (J_c) for HEA SC thin films at 2.0 and 4.2 K, respectively. All the films show remarkably large J_c values at 0 T compared with that of the bulk HEA SC sample, as well as promising field performance. The low-field J_c at 2.0 K is lower than that at 4.2 K because of the considerable flux jump at 2.0 K. The red dashed line marks $J_c = 100$ kA cm $^{-2}$, which is a common benchmark for large-scale applications such as high-field SC magnets. **c** Relative levels of J_c at 2.0 and 4.2 K at 1 T show that HEA superconductors are available for widespread applications.

Effect of ion irradiation on HEA SC thin films. Robust superconductivity with respect to disorder has been proposed on the basis of experimental observations of the insensitivity of the T_c of HEA superconductors to the disorder introduced by different levels of constituent atoms^{16,34}. In addition, the stable superconductivity of HEAs containing the radioactive element U

makes HEA superconductors promising for application in heavy-irradiation environments, such as in aerospace applications and nuclear fusion^{6,7}. However, to the best of our knowledge, no studies have investigated the effect of ion irradiation on HEA superconductors. To examine the stability of the SC phase of HEAs against irradiation damage, high-quality HEA SC thin films

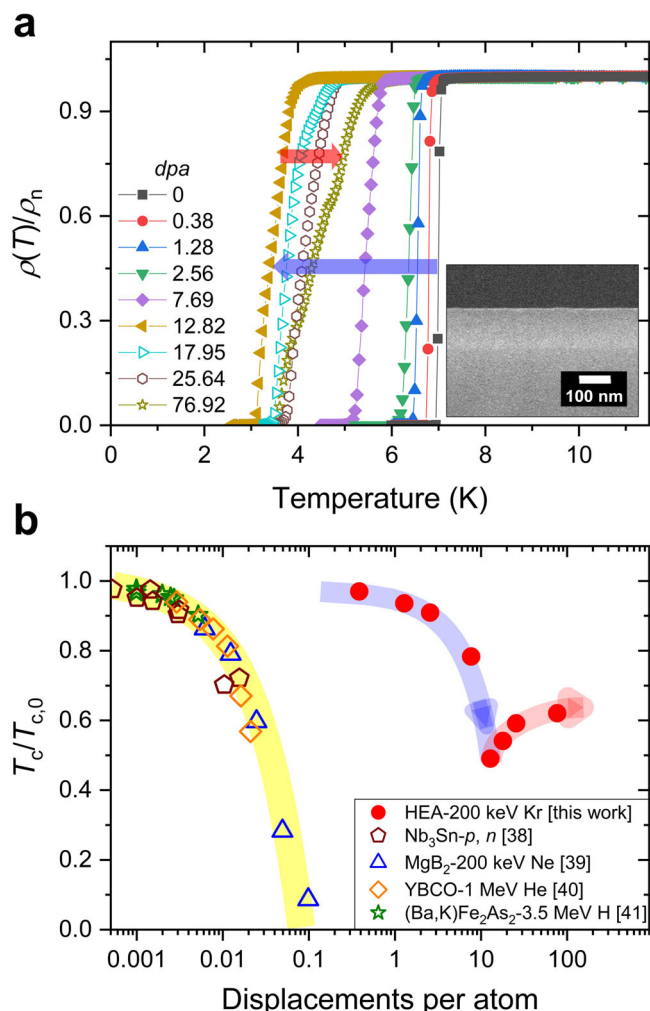


Fig. 4 Changes in SC transition temperature for HEA SC thin films against irradiation damage. **a** $\rho(T)$ curves near T_c for the 200 keV Kr-ion-irradiated Ta-Nb-Hf-Zr-Ti HEA SC thin films with a thickness of 115 nm, where $\rho(T)$ was normalized by ρ_n for comparison. The T_c of HEA SC thin films decreases gradually with an increase in dpa , but for $dpa > 12.82$ (left triangles), strikingly, the T_c exhibits an increase despite the increase in the dpa level (see the arrow direction). **b** $T_c/T_{c,0}$ with respect to dpa for representative SC materials with potential for practical applications, where $T_{c,0}$ represents the T_c of the pristine sample and p and n for Nb₃Sn indicate proton irradiation and neutron irradiation, respectively. The Ta-Nb-Hf-Zr-Ti HEA SC thin films show a remarkably robust superconductivity against irradiation-induced disorder compared with that of the other SC materials. Half-transparent shades are guides to the eyes.

were systematically irradiated with low-energy 200 keV Kr ions^{35–37}. Figure 4a shows the $\rho(T)$ curves for the irradiated Ta-Nb-Hf-Zr-Ti HEA SC thin films with a thickness of 115 nm, where $\rho(T)$ was normalized by ρ_n for comparison. The inset of Fig. 4a presents a cross-sectional SEM image used for ion irradiation. The disorder levels were adjusted using amounts of irradiated Kr ions from 1.5×10^{14} to 3×10^{16} Kr ions cm^{-2} , corresponding to displacements per atom (dpa) from 0.38 to 76.92 (see Supplementary Fig. 8). The superconductivity of the HEA SC thin film was remarkably resistant to the displacement damage produced by irradiation. The T_{cR} of 7.0 K for the pristine film decreased gradually as the level of dpa increased, but remained at 3.4 K at $dpa = 12.82$. For further increases in the dpa level, strikingly, the T_{cR} showed an increase rather than a decrease and reached 4.3 K at the extreme damage level of $dpa = 76.92$.

Figure 4b shows a plot of T_c as a function of dpa for Ta-Nb-Hf-Zr-Ti HEA SC thin films and other superconductors with potential for practical application, such as Nb₃Sn³⁸, MgB₂³⁹, YBa₂Cu₃O_{7-x}⁴⁰, and K-doped BaFe₂As₂⁴¹. Here, T_c was normalized to the T_c of each pristine sample ($T_{c,0}$) for comparison. With an increase in the dpa value, T_c decreased monotonically and is expected to be completely suppressed below $dpa = 1$ for the other superconductors. However, the range of the dpa values for the HEA SC thin films differed significantly from those for the other superconductors: the superconductivity of the HEA SC thin films was over 1000 times more resistant to displacement damage than that of the other superconductors. The suppression of T_c in crystalline SC materials against dpa is generally considered to be a result of the disorder effect associated with SC gap pairing symmetry and the degradation of crystallinity due to atomic disorder^{38,42}. In contrast, the extraordinarily stable SC phase of HEAs against irradiation-induced disorder could be related to the occurrence of amorphization-recrystallization and the high interstitial-vacancy recombination rate associated with the high atomic-level stress and/or high-level lattice distortion in HEAs resulting from their high configuration entropy^{3,43–45}. In addition, the random occupation of lattice sites of the constituent atoms of HEAs seems related to the robust superconductivity of HEAs against irradiation damage, because the atomic positions in the lattice altered by the recombination may have little effect on the characteristic of HEAs¹⁶. Our irradiation study of Ta-Nb-Hf-Zr-Ti HEA SC thin films manifests the excellent robustness of the SC phase against irradiation damage, which is expected to open the door to many potential applications of HEA superconductors.

In summary, we fabricated high-quality Ta-Nb-Hf-Zr-Ti HEA SC thin films using the PLD method. A large critical current density of $J_c > 1 \text{ MA cm}^{-2}$ was realized, and a J_c of 0.1 MA cm^{-2} —a common benchmark for large-scale application—was maintained under magnetic fields of approximately 3.4 and 2.0 T at 2.0 and 4.2 K, respectively. In addition, the superconductivity of the HEA SC thin films was over 1000 times more robust to displacement damage than that of other representative SC materials, such as Nb₃Sn, MgB₂, Fe-based superconductors, and high- T_c cuprates. Taken together with the wide range of growth temperatures for high-quality thin films, these results demonstrate the great potential of HEA superconductors for practical applications under various extreme environments, such as aerospace applications, high-field SC magnets, and irradiation environments.

Methods

Fabrication of Ta-Nb-Hf-Zr-Ti HEA SC thin films. A Ta_{1/6}Nb_{2/6}Hf_{1/6}Zr_{1/6}Ti_{1/6} HEA SC target with a diameter of 15 mm and bulk samples A and B were prepared using a planetary ball-milling (FRITSCH GmbH, PULVERISETTE 5, Germany) and hot-press sintering process³. Ta (99.98%), Nb (99.8%), Hf (99.6%), Zr (99.5%), and Ti (99.5%) powders with a compositional ratio of 1:2:1:1:1 were loaded in a stainless-steel jar equipped with a stainless-steel ball in an Ar atmosphere to prevent oxidation. Ball milling with a ball to HEA powder ratio of 10: 1 was performed at a rotation speed of 400 rpm for 24 h using a planetary ball milling machine, after which the powder was sintered via a hot-press sintering method at 1000 °C for 1 h under a uniaxial pressure of 50 MPa.

High-quality Ta-Nb-Hf-Zr-Ti HEA SC thin films were fabricated on *c*-cut Al₂O₃ substrates (10 mm × 10 mm) using a PLD technique. The laser beam was generated using a KrF excimer laser ($\lambda = 248 \text{ nm}$, IPEX864; LightMachinery) and the thin films were deposited using a laser energy density of $\sim 3.85 \text{ J cm}^{-2}$ and a repetition rate of 10 Hz in a high vacuum state of $\sim 10^{-6}$ Torr. Thin films were fabricated with substrate temperatures (T_s) ranging from 270 to 620 °C, and all the films exhibited superconductivity. By controlling the growth time, we obtained Ta-Nb-Hf-Zr-Ti HEA SC thin films with thicknesses in the range of 115–700 nm.

Ion irradiation and characterization of thin films. Kr ions with a beam energy of 200 keV were used to irradiate Ta-Nb-Hf-Zr-Ti HEA SC thin films with a thickness of 115 nm at the Korea Multi-Purpose Accelerator Complex (KOMAC) in Gyeongju. Kr ion levels of 1.5×10^{14} , 5×10^{14} , 1×10^{15} , 3×10^{15} , 5×10^{15} , 7×10^{15} , 1×10^{16} , and 3×10^{16} Kr ions cm^{-2} were irradiated onto the films at room

temperature, with a tilt angle of 7° to avoid channeling effects during the irradiation. The displacement damage produced in the $\text{Ta}_{1/6}\text{Nb}_{2/6}\text{Hf}_{1/6}\text{Zr}_{1/6}\text{Ti}_{1/6}$ HEA superconductor (density of 9.9 g cm^{-3}) by the 200 keV Kr-ion irradiation was estimated using the Stopping and Range of Ions in Matter (SRIM) Monte Carlo simulation program with averaged displacement threshold energy values of 90 eV (Ta), 78 eV (Nb), 61 eV (Hf), 40 eV (Zr), and 30 eV (Ti)^{46,47}. The simulated target displacement values from the SRIM program were converted into displacements per atom (*dpa*) values using the following relationship (see also Supplementary Fig. 8):

$$\frac{\text{displacements}}{\text{atom} \times \text{\AA}} \times \frac{10^8 (\text{\AA}/\text{cm}) \times \text{dose} (\text{atoms}/\text{cm}^2)}{\rho_{\text{HEA}} \left(\frac{\text{atoms}}{\text{cm}^3} \right)} = \frac{\text{displacements}}{\text{atom}} = \text{dpa}, \quad (2)$$

where $\rho_{\text{HEA}} = 5.226 \times 10^{22} \text{ atoms cm}^{-3}$ is the atomic density of $\text{Ta}_{1/6}\text{Nb}_{2/6}\text{Hf}_{1/6}\text{Zr}_{1/6}\text{Ti}_{1/6}$. The doses 1.5×10^{14} , 5×10^{14} , 1×10^{15} , 3×10^{15} , 5×10^{15} , 7×10^{15} , 1×10^{16} , and 3×10^{16} Kr ions cm^{-2} corresponded to *dpa* values of 0.38, 1.28, 2.56, 7.69, 12.82, 17.95, 25.64, and 76.92, respectively.

The crystal structure of the fabricated Ta–Nb–Hf–Zr–Ti HEA SC thin films was investigated using an X-ray diffractometer (Rigaku miniflex-600 diffractometer, Cu-K α_1 radiation, $\lambda = 1.541 \text{ \AA}$). The thicknesses and compositional ratios of the thin films were examined using scanning electron microscope and energy-dispersive X-ray spectrometry, respectively. The SC transition temperature (T_c) of the fabricated Ta–Nb–Hf–Zr–Ti HEA SC thin films was evaluated from the temperature dependence of the electrical resistivity (ρ) and magnetization (M) using a physical property measurement system (PPMS 9 T, Quantum Design) and a magnetic property measurement system (MPMS 5 T, Quantum Design), respectively. The $\rho(T)$ was measured using the standard four-probe method with an Au coating on the four-point contact regions to achieve good ohmic contact, and the upper critical field ($\mu_0 H_{c2}$) was estimated by measuring the $\rho(T)$ curve in the magnetic field from 0 to 9 T in the PPMS. The critical current density (J_c) of the HEA SC thin films as a function of the magnetic field was calculated from the magnetization hysteresis (M – H) loops based on Bean's critical state model ($J_c = 15\Delta M/rV$) (see Supplementary Fig. 7). Here, the M – H loops were measured using MPMS, and ΔM is the difference in M values at the same magnetic field in the M – H loops, V is the volume of the film, and r is the radius corresponding to the total area of the surface of the film⁴⁸. The direction of the magnetic field was perpendicular to the *ab* plane of the film for $H_{c2}(T)$ and $J_c(H)$.

Data availability

The authors declare that all the data supporting the finding of this study are available within this article and its Supplementary Information files and are available from the corresponding author on reasonable request.

Received: 19 January 2022; Accepted: 6 May 2022;

Published online: 11 June 2022

References

1. Yeh, J.–W. et al. Nanostructured high-entropy alloys with multiple principal elements: Novel alloy design concepts and outcomes. *Adv. Eng. Mater.* **6**, 299–303 (2004).
2. Sun, L. & Cava, R. J. High-entropy alloy superconductors: Status, opportunities, and challenges. *Phys. Rev. Mater.* **3**, 090301 (2019).
3. Wang, X., Guo, W. & Fu, Y. High-entropy alloys: Emerging materials for advanced functional applications. *J. Mater. Chem. A* **9**, 663–701 (2021).
4. Kitagawa, J., Hamamoto, S. & Ishizu, N. Cutting edge of high-entropy alloy superconductors from the perspective of materials research. *Metals* **10**, 1078 (2020).
5. Guo, J. et al. Robust zero resistance in a superconducting high-entropy alloy at pressures up to 190 GPa. *Proc. Natl Acad. Sci. USA* **114**, 13144–13147 (2017).
6. Shi, T. et al. Current development of body-centered cubic high-entropy alloys for nuclear applications. *Tungsten* **3**, 197–217 (2021).
7. Nelson, W. L. et al. Superconductivity in a uranium containing high entropy alloy. *Sci. Rep.* **10**, 4717 (2020).
8. Chen, S. et al. Simultaneously enhancing the ultimate strength and ductility of high-entropy alloys via short-range ordering. *Nat. Commun.* **12**, 4953 (2021).
9. Anderson, P. W., Muttalib, K. A. & Ramakrishnan, T. V. Theory of the “universal” degradation of T_c in high-temperature superconductors. *Phys. Rev. B* **28**, 117–120 (1983).
10. Kirkpatrick, T. R. & Belitz, D. Suppression of superconductivity by disorder. *Phys. Rev. Lett.* **68**, 3232–3235 (1992).
11. George, E. P., Curtin, W. A. & Tasan, C. C. High entropy alloys: A focused review of mechanical properties and deformation mechanisms. *Acta Mater.* **188**, 435–474 (2020).
12. Loa, I., Kunc, K., Syassen, K. & Bouvier, P. Crystal structure and lattice dynamics of AlB_2 under pressure and implications for MgB_2 . *Phys. Rev. B* **66**, 134101 (2002).
13. Kim, G. et al. Strongly correlated and strongly coupled s-wave superconductivity of the high entropy alloy $\text{Ta}_{1/6}\text{Nb}_{2/6}\text{Hf}_{1/6}\text{Zr}_{1/6}\text{Ti}_{1/6}$ compound. *Acta Mater.* **186**, 250–256 (2020).
14. Mizuguchi, Y., Kasem, M. R. & Matsuda, T. D. Superconductivity in CuAl_2 -type $\text{Co}_{0.2}\text{Ni}_{0.1}\text{Cu}_{0.1}\text{Rh}_{0.3}\text{Ir}_{0.3}\text{Zr}_2$ with a high-entropy-alloy transition metal site. *Mater. Res. Lett.* **9**, 141–147 (2021).
15. Zhang, X., Winter, N., Witteveen, C., Moehl, T. & Xiao, Y. Preparation and characterization of high-entropy alloy $(\text{TaNb})_{1-x}(\text{ZrHfTi})_x$ superconducting films. *Phys. Rev. Res.* **2**, 013375 (2020).
16. von Rohr, F., Winiarski, M. J., Tao, J., Klimczuk, T. & Cava, R. J. Effect of electron count and chemical complexity in the Ta–Nb–Hf–Zr–Ti high-entropy alloy superconductor. *Proc. Natl Acad. Sci. USA* **113**, E7144–E7150 (2016).
17. Ghorbani, S. R. et al. Flux pinning and vortex transitions in doped BaFe_2As_2 single crystals. *Appl. Phys. Lett.* **100**, 072603 (2012).
18. Jung, S.–G. et al. Influence of carbon-ion irradiation on the superconducting critical properties of MgB_2 thin films. *Supercond. Sci. Technol.* **32**, 025006 (2019).
19. Fisher, D. S., Fisher, M. P. A. & Huse, D. A. Thermal fluctuations, quenched disorder, phase transitions, and transport in type-II superconductors. *Phys. Rev. B* **43**, 130–159 (1991).
20. Kwok, W. K., Fendrich, J. A., van der Beek, C. J. & Crabtree, G. W. Peak effect as a precursor to vortex lattice melting in single crystal $\text{YBa}_2\text{Cu}_3\text{O}_{7-\delta}$. *Phys. Rev. Lett.* **73**, 2614–2617 (1994).
21. Werthamer, N. R., Helfand, E. & Hohenberg, P. C. Temperature and purity dependence of the superconducting critical field, H_{c2} . III. Electron spin and spin-orbit effects. *Phys. Rev.* **147**, 295–302 (1966).
22. Bose, S., Raychaudhuri, P., Banerjee, R. & Ayyub, P. Upper critical field in nanostructured Nb: Competing effects of the reduction in density of states and the mean free path. *Phys. Rev. B* **74**, 224502 (2006).
23. Niu, H. J. & Hampshire, D. P. Disordered nanocrystalline superconducting PbMo_6S_8 with a very large upper critical field. *Phys. Rev. Lett.* **91**, 027002 (2003).
24. Cooley, L. D. & Motowidlo, L. R. Advances in high-field superconducting composites by addition of artificial pinning centres to niobium–titanium. *Supercond. Sci. Technol.* **12**, R135–R151 (1999).
25. Nishigaki, K. & Takeda, M. Influence of thickness on parallel and perpendicular field dependences of J_c of NbTi films. *Physica C* **357–360**, 1373–1376 (2001).
26. Boutboul, T., Naour, S. L., Leroy, D., Oberli, L. & Previtali, V. Critical current density in superconducting Nb–Ti strands in the 100 mT to 11 T applied field range. *IEEE Trans. Appl. Supercond.* **16**, 1184–1187 (2006).
27. Xu, S. Y. et al. High critical current density and vortex pinning of epitaxial MgB_2 thin films. *Phys. Rev. B* **68**, 224501 (2003).
28. Talantsev, E. F., Crump, W. P. & Tallon, J. L. Universal scaling of the self-field critical current in superconductors: From sub-nanometre to millimeter size. *Sci. Rep.* **7**, 10010 (2017).
29. Talantsev, E. F., Crump, W. P. & Tallon, J. L. Thermodynamic parameters of single- or multi-band superconductors derived from self-field critical currents. *Ann. Phys.* **529**, 1700197 (2017).
30. Denisov, D. V. et al. Onset of dendritic flux avalanches in superconducting films. *Phys. Rev. Lett.* **97**, 077002 (2006).
31. Bag, P., Su, Y.–C., Kuo, Y.–K., Lai, Y.–C. & Wu, S.–K. Physical properties of face-centered cubic structured high-entropy alloys: Effects of NiCo, NiFe, and NiCoFe alloying with Mn, Cr, and Pd. *Phys. Rev. Mater.* **5**, 085003 (2021).
32. Choi, E.–M. et al. Enhancement at low temperatures of the critical current density for Au-coated MgB_2 thin films. *Appl. Phys. Lett.* **84**, 82–84 (2004).
33. Larbalestier, D., Gurevich, A., Feldmann, D. M. & Polyanskii, A. High- T_c superconducting materials for electric power applications. *Nature* **414**, 368–377 (2001).
34. von Rohr, F. O. & Cava, R. J. Isoelectronic substitutions and aluminium alloying in the Ta–Nb–Hf–Zr–Ti high-entropy alloy superconductor. *Phys. Rev. Mater.* **2**, 034801 (2018).
35. Jung, S.–G. et al. Field-induced quantum breakdown of superconductivity in magnesium diboride. *NPG Asia Mater.* **13**, 55 (2021).
36. Parkin, D. M. Radiation effects in high-temperature superconductors: A brief review. *Metal. Trans. A* **21A**, 1015–1019 (1990).
37. Nordlund, K. et al. Defect production in collision cascades in elemental semiconductors and fcc metals. *Phys. Rev. B* **57**, 7556–7570 (1998).
38. Flükiger, R. et al. Variation of T_c , lattice parameter and atomic ordering in Nb_2Sn platelets irradiated with 12 MeV protons: Correlation with the number of induced Frenkel defects. *Supercond. Sci. Technol.* **30**, 054003 (2017).
39. Lee, J. M. et al. Influence of disorder strength on the superconducting mechanism of MgB_2 . *Supercond. Sci. Technol.* **35**, 015001 (2022).

40. Lesueur, J., Dumoulin, L., Quillet, S. & Radcliffe, J. Ion-beam induced metal insulator transition in YBCO films. *J. Alloy. Compd.* **195**, 527–530 (1993).
41. Torsello, D., Gozzelino, L., Gerbaldo, R., Tamegai, T. & Ghigo, G. Scaling laws for ion irradiation effects in iron-based superconductors. *Sci. Rep.* **11**, 5818 (2021).
42. Andersen, L., Ramires, A., Wang, Z., Lorenz, T. & Ando, Y. Generalized Anderson's theorem for superconductors derived from topological insulators. *Sci. Adv.* **6**, eaay6502 (2020).
43. Zhang, Z., Armstrong, D. E. J. & Grant, P. S. The effects of irradiation on CrMnFeCoNi high-entropy alloy and its derivatives. *Prog. Mater. Sci.* **123**, 100807 (2022).
44. Egami, T., Guo, W., Rack, P. D. & Nagase, T. Irradiation resistance of multicomponent alloys. *Metall. Mater. Trans. A* **45**, 180–183 (2014).
45. Nagase, T., Rack, P. D., Noh, J. H. & Egami, T. In-situ TEM observation of structural changes in nano-crystalline CoCrCuFeNi multicomponent high-entropy alloy (HEA) under fast electron irradiation by high voltage electron microscopy (HVEM). *Intermetallics* **59**, 32–42 (2015).
46. Konobeyev, A. Y., Fischer, U., Korovin, Y. A. & Simakov, S. P. Evaluation of effective threshold displacement energies and other data required for the calculation of advanced atomic displacement cross-sections. *Nucl. Eng. Technol.* **3**, 169–175 (2017).
47. The damage events by 200 keV Kr-ion irradiation in the Ta–Nb–Hf–Zr–Ti SC thin film were calculated using the SRIM software. (www.srim.org/).
48. Kim, H.-J. et al. High current-carrying capability in *c*-axis-oriented superconducting MgB₂ thin films. *Phys. Rev. Lett.* **87**, 087002 (2001).

Acknowledgements

We wish to acknowledge the outstanding support of the accelerator group and operators of KOMAC, KAERI. This study was supported by the National Research Foundation (NRF) of Korea through a grant funded by the Korean Ministry of Science and ICT (No. 2021R1A2C2010925 (T.P. and Y.H.) and 2021R1A2C20121340 (W.S.C.)) and by the Basic Science Research Program through the NRF of Korea funded by the Ministry of Education (NRF-2019R1F1A1055284 (J.M.L. and W.N.K.), NRF-2020R1I1A1A01067677 (J.H.K.), and NRF-2021R1I1A1A01043885 (S.-G.J. and Y.H.)).

Author contributions

S.-G.J. conceived the study. S.-G.J. and Y.H. fabricated the high-quality Ta–Nb–Hf–Zr–Ti HEA superconducting thin films and performed transport and magnetization measurements.

J.H.K., R.H., and J.-S.R. prepared an HEA superconducting target and bulk samples. H.J., J.S., S.-G.J., and Y.H. performed Kr-ion irradiation. J.M.L., W.N.K., and W.S.C. assisted with the pulsed laser deposition. S.-G.J. and Y.H. analyzed the data. The manuscript was written by Y.H., S.-G.J., and T.P., with contributions from all authors.

Competing interests

The authors declare no competing interests.

Additional information

Supplementary information The online version contains supplementary material available at <https://doi.org/10.1038/s41467-022-30912-5>.

Correspondence and requests for materials should be addressed to Soon-Gil Jung or Tuson Park.

Peer review information *Nature Communications* thanks Liling Sun, Jiro Kitagawa and the other anonymous reviewers for their contribution to the peer review of this work.

Reprints and permission information is available at <http://www.nature.com/reprints>

Publisher's note Springer Nature remains neutral with regard to jurisdictional claims in published maps and institutional affiliations.



Open Access This article is licensed under a Creative Commons Attribution 4.0 International License, which permits use, sharing, adaptation, distribution and reproduction in any medium or format, as long as you give appropriate credit to the original author(s) and the source, provide a link to the Creative Commons license, and indicate if changes were made. The images or other third party material in this article are included in the article's Creative Commons license, unless indicated otherwise in a credit line to the material. If material is not included in the article's Creative Commons license and your intended use is not permitted by statutory regulation or exceeds the permitted use, you will need to obtain permission directly from the copyright holder. To view a copy of this license, visit <http://creativecommons.org/licenses/by/4.0/>.

© The Author(s) 2022